

Multi-Step Crystallization and Chemical Evolution of Sodium Yttrium Fluoride

Peter Pauzauskie (✉ peterpz@uw.edu)

University of Washington <https://orcid.org/0000-0002-1554-5949>

Alexander Bard

University of Washington

R. Greg Felsted

University of Washington

Abbie Ganas

University of Washington

Anupum Pant

University of Washington

Chaman Gupta

University of Washington

Ying Chen

Pacific Northwest National Laboratory <https://orcid.org/0000-0001-7417-0991>

Elias Nakouzi

Pacific Northwest National Laboratory

Biao Jin

Pacific Northwest National Laboratory

Nancy Washton

Environmental Molecular Sciences Laboratory

James De Yoreo

Pacific Northwest National Laboratory <https://orcid.org/0000-0002-9541-733X>

Jaehun Chun

Pacific Northwest National Laboratory <https://orcid.org/0000-0002-2291-6496>

Lucien Brush

University of Washington

Physical Sciences - Article

Keywords:

Posted Date: December 3rd, 2021

DOI: <https://doi.org/10.21203/rs.3.rs-1097450/v1>

License:  This work is licensed under a Creative Commons Attribution 4.0 International License.

[Read Full License](#)

1 Multi-Step Crystallization and Chemical Evolution of 2 Sodium Yttrium Fluoride

3 Alexander B. Bard,^{1†} R. Greg Felsted,^{1†} Abbie S. Ganas,¹ Anupum Pant,² Chaman Gupta,² Ying
4 Chen,³ Elias Nakouzi,⁴ Biao Jin,⁴ Nancy M. Washton,⁴ James J. De Yoreo,^{1,2,4} Jaehun Chun,⁴
5 Lucien N. Brush,² and Peter J. Pauzauskie^{2,4*}

6 ¹*Department of Chemistry, University of Washington, Seattle, Washington 98195*

7 ²*Department of Materials Science and Engineering, University of Washington, Seattle, WA 98195*

8 ³*Environmental Molecular Sciences Laboratory, Pacific Northwest National Laboratory, Richland,*
9 *WA 99354*

10 ⁴*Physical Sciences Division, Physical & Computational Sciences Directorate, Pacific Northwest*
11 *National Laboratory, Richland, Washington 99352*

12 † These authors contributed equally to this work

13 Abstract

14 **Two-step crystallization mechanisms based on spinodal decomposition followed by nucle-**
15 **ation are commonly observed both in the laboratory and in nature.^{1,2} While this pathway**
16 **may require chemical reactions, subsequent nucleation and growth are often considered as**
17 **separate, discrete events from the reaction itself.³ Recent work has also shown a distinct in-**
18 **termediate step involving the formation of an amorphous aggregate.⁴ Here we report a novel**
19 **four-step mechanism in the aqueous synthesis of sodium yttrium fluoride involving 1) the**
20 **segregation of aqueous ions into a dense liquid phase, 2) the formation of an amorphous ag-**
21 **gregate, 3) nucleation of a cubic YF_3 phase, and 4) subsequent solid-state diffusion of sodium**
22 **and fluoride ions to form a final NaYF_4 phase. The final step involves a continuous, gradual**
23 **change of the solid phase's chemical stoichiometry from YF_3 toward NaYF_4 . Unlike previ-**
24 **ously studied nucleation and growth mechanisms, the stoichiometry of the final solid phase**
25 **evolves throughout the crystallization process rather than being determined at nucleation.**
26 **This novel four-step mechanism provides a new perspective into the nucleation and growth**
27 **of many other crystalline materials given the ubiquity of nonstoichiometric compounds in**
28 **nature.**

29 Introduction

30 Classical nucleation theory (CNT), first described by Gibbs over 140 years ago, has been a robust
31 model for describing the formation of crystals from a homogeneous solution.⁵ However, despite
32 its simplicity and general validity for many crystallization processes, some proceed via so-called
33 "nonclassical" mechanisms.⁶⁻⁸ These mechanisms include, but are not limited to, the formation of
34 amorphous or poorly-crystalline species and the oriented aggregation and attachment of individual
35 building blocks.⁶ Broadly speaking, nonclassical crystallization is a realization of Ostwald's step

36 rule, which suggests that systems will not necessarily take the most direct route to their most stable
37 phase, but rather that they tend to go through a series of intermediates that are closer in free energy
38 to the initial state.^{9,10}

39 One such nonclassical crystallization mechanism is two-step nucleation via a dense liquid
40 phase (DLP), typically formed through spinodal decomposition (SD).^{11,12} In this mechanism, the
41 highly supersaturated initial phase spontaneously separates free of a thermodynamic energy bar-
42 rier¹³ into ion-rich and ion-poor liquid phases, and crystals then nucleate from the ion-rich phase,
43 possibly via an amorphous intermediate.¹ This mechanism has been observed directly via liq-
44 uid cell transmission electron microscopy (TEM) of gold nucleation from solution¹ as well as in
45 electrochemical reactions in nanoparticles,¹⁴ in molecular dynamics (MD)¹² and kinetic studies
46 of calcium carbonate,² in bulk chemical studies of MgSO₄ at high temperature,¹⁵ by optical mi-
47 croscopy in crystallizable polymer solutions,¹⁶ in MD simulations of highly supersaturated NaCl
48 solutions,¹⁷ and in optical microscopy and light scattering studies of protein solutions.¹¹ Some sys-
49 tems have also shown a distinct intermediate step in which the DLP condenses into an amorphous
50 phase prior to crystallization.⁴ These studies, among others,¹⁸ suggest that the two-step mechanism
51 via a DLP can readily be accessed in a wide range of solution-based systems, because, when taken
52 to sufficiently high supersaturation, nearly all solutions will reach their limit of stability.¹⁹

53 One aspect of these two-step pathways via a DLP that remains largely unexplored is that
54 the stoichiometry of the intermediate phase is variable and ill-defined and must evolve to generate
55 the final stable phase. This is because the compositions of the ion-rich and ion-poor liquids are
56 defined by a phase line that traverses a range of compositions rather than by a set of line com-
57 pounds. Therefore, for crystallization to proceed, ions must be rejected from or drawn into the
58 solidifying regions of the ion-rich liquid droplets. This adds a level of complexity to other previ-
59 ously investigated nonclassical systems, in which the intermediate phases are all line compounds,

60 which can either be identical for each phase, for example, as in the case of CaCO_3 (ignoring waters
61 of hydration), or they can be distinct and require chemical transformation, as documented for the
62 calcium phosphate system.²⁰ For the latter, charged calcium triphosphate species undergo aggre-
63 gation accompanied by Ca^{2+} binding and deprotonation to create the amorphous phase, and then
64 undergo a second step of Ca^{2+} binding and deprotonation to create the first crystalline phase. In a
65 DLP-mediated pathway, on the other hand, ions may exchange more dynamically rather than via
66 specific transformations to these discrete line compounds. The added complexity in these two-step
67 pathways is further emphasized when the final compound has a ternary or more complex stoi-
68 chiometry, which increases the difficulty of the required ionic reorganization. Given the common
69 occurrence of the formation of DLPs in highly supersaturated solutions and the preponderance of
70 ternary and more complex compounds in natural and synthetic systems, this motivates the further
71 study of the chemical evolution of intermediate phases in these systems.

72 Here we investigate this multi-step crystal growth pathway using a model system based on
73 ternary sodium-yttrium-fluoride (NaYF) materials. This is an ideal system for exploring the role
74 of chemical evolution during crystallization because the stoichiometry of NaYF materials has been
75 shown²¹ to vary as a combination of NaF and YF_3 that varies continuously with a final stoichiome-
76 try of $\text{Na}_{0.5-x}\text{Y}_{0.5+x}\text{F}_{2+2x}$, or $(0.5-x)\text{NaF} \cdot (0.5+x)\text{YF}_3$, with $0 < x < 0.5$. When $x = 0$, the stoichiometry
77 becomes NaYF_4 , which is used frequently as shorthand for this material. Due to the importance of
78 the variable stoichiometry of this system to our paper, we instead use the shorthand NaYF when re-
79 ferring to this material. The majority of aqueous syntheses of NaYF use either microemulsion sol-
80 vent systems²² or organic capping ligands²³ for the purpose of controlling both the size and shape
81 of discrete nanocrystals²⁴. In this work we synthesized ligand-free NaYF materials to provide a
82 clear understanding of the role of solvated aqueous ion dynamics by eliminating ion chelation and
83 surface passivation by organic species. Our results demonstrate the formation of a novel DLP in the
84 NaYF system through a two-step mechanism, followed by a third step of solid-state diffusion that

85 determines the final stoichiometry of the material. This change in stoichiometry has not previously
86 been studied in systems that proceed by SD. Further investigation of this mechanism could also
87 lead to the development of many functional materials. For example, the fundamental insights into
88 the multi-step nucleation and growth of materials that display nonstoichiometry in nature could
89 lead to advances in the design of materials for a diverse range of applications including photody-
90 namic therapy,²⁵ solid-state laser refrigeration,²⁶ optical thermometry²⁷, nanoscale lasing²⁸, night
91 vision²⁹, and electrochemical energy storage^{30,31}.

92 **Results and Discussion**

93 In order to probe the nucleation and growth of NaYF materials in the absence of organic ligands we
94 first prepared aqueous electrolyte solutions of both NaF and YF₃, and then combined them at stan-
95 dard conditions with relative concentrations stoichiometric to NaYF₄ (Figure 1A). Immediately
96 upon mixing the starting solutions, we observed the apparent formation of a gel-like material (Fig-
97 ure 1B), which can be filtered to a translucent solid (Figure 1C). This gel remains relatively stable
98 for several hours, after which it begins to collapse into a white powder (Figure S1). TEM imaging
99 of the gel shows an interconnected, porous structure (Figure 1D). Scanning TEM (STEM) tomog-
100 raphy reveals not only the interconnected three-dimensional morphology (Figure 1F) but also the
101 open-cell structure that can't be seen in conventional STEM (Figure 1G). Brunauer-Emmett-Teller
102 (BET) surface area measurements show a surface area of the gel phase on the order of 100 m²/g,
103 and powder X-ray diffraction (XRD) data show very broad peaks consistent with α -NaYF or a
104 similar cubic material (Figure S2). To the best of our knowledge there has been one previous
105 observation of interconnected particle morphology during the aqueous synthesis of NaYF materi-
106 als.³² However, to date there has been neither discussion of the unusual multi-step gel formation
107 mechanism nor detailed microstructural characterization of the recovered gel material reported in
108 the literature.

109 While the XRD data were consistent with nanocrystalline α -NaYF (Figure S2), the peaks
110 were not sufficiently resolved to be able to definitively conclude that the gel is purely α -NaYF.
111 To further complicate the analysis of these data, TEM data suggest that there are some amor-
112 phous, poorly crystalline, or otherwise disordered regions (Figure 2D). Furthermore, we observe
113 beam-induced crystallization in the TEM (Figure S3), which suggests that the high resolution TEM
114 (HRTEM) is in fact underestimating the distribution of the amorphous and poorly crystalline mate-
115 rial. However, under the assumption that any crystals that are induced by the beam in vacuum will
116 have the same composition as their disordered precursor, we can use this beam-induced crystalliza-
117 tion to estimate the local composition of the material. Using custom fast Fourier transform (FFT)
118 indexing software (Figure 2E), we were able to show that most regions of the gel contain an FFT
119 peak between 3.00 and 3.16 Å. This was indexed to the (111) plane of a cubic NaF–YF₃ structure,
120 with smaller d-spacings corresponding to a more NaF-rich structure (more similar to NaYF₄, fig-
121 ure 2A), and larger d-spacings corresponding to a more NaF-poor structure (more similar to cubic
122 YF₃, figure 2B). This analysis shows relatively smooth fluctuations between compositional states,
123 showing that the NaF–YF₃ ratio is not constant in the recovered gel and that it should be thought
124 of as in a composition between YF₃ and NaYF₄. The measured d-spacings are shifted from litera-
125 ture values for the (111) planes of cubic NaYF₄ and YF₃ due to approximations in measuring the
126 scale bar, but the individual spots are accurate relative to each other, and therefore the trend is not
127 affected. A histogram of the detected d-spacings can be found in Figure S4. It should be noted
128 that the thermodynamically stable orthorhombic structure of YF₃ (Figure 2C) was not observed in
129 the gel. Considering the crystal structures of these two phases, it is notable that they share a nearly
130 identical lattice of fluoride ions (though each unit cell of the YF₃ contains an extra fluoride ion at
131 the center), but that the corners of the YF₃ unit cell are unoccupied, which results in large channels
132 that run through the entire crystal structure. We propose that these channels readily allow for the
133 diffusion of ions into the lattice, allowing for local variations in stoichiometry. This is consistent
134 with much of the literature regarding cubic NaF–YF₃ structures grown from melt insofar as that the

135 bulk material can be thought of as a solid solution of NaF and YF_3 .^{21,33} However, to our knowl-
136 edge, this has not been thoroughly characterized on the nanoscale, nor has any mechanism been
137 described for its structural evolution in solution-phase syntheses.

138 We hypothesize that the gel initially forms both amorphous and cubic domains of YF_3 while
139 the excess NaF in solution slowly incorporates into the matrix to form the more stable cubic NaYF
140 phase. We do not observe distinct XRD peaks for YF_3 and NaYF₄ in recovered gel materials due
141 to the effects of nonstoichiometry and Scherrer broadening. To investigate the gradual transition
142 from YF_3 to NaYF, we attempted a cation substitution experiment on the gel using monovalent
143 potassium cations. By removing the gel from its native solution as shown previously, it is possible
144 to suspend temporarily the process of monovalent sodium ion incorporation. After submerging the
145 recovered NaYF gel in a concentrated (1M) KF solution, we observe that the remaining sodium-
146 poor regions incorporate KF to form KY_3F_{10} (KYF) (Figure 3A), which is distinguishable in XRD
147 after the gel is allowed to fully collapse into single crystals (Figure 3B). While KYF can form in
148 multiple stoichiometries, the KY_3F_{10} stoichiometry forms in this case because it is stable in the
149 cubic crystal phase and has the lowest potassium / yttrium ion ratio.³⁴ By varying the amount of
150 time spent incubating in the native solution before filtering and transferring to the KF solution (t_{inc}),
151 we can observe how much sodium has incorporated into the gel in that time and how much YF_3
152 remains, which we can observe after converting to KYF. As t_{inc} increases from 15 minutes to two
153 hours, we observe the proportion of the sodium phase to increase linearly with a corresponding
154 linear decrease in the relative amount of material that incorporates potassium (Figure 3C). This
155 shows that the incorporation of sodium into the crystal structure occurs as the result of solid-state
156 diffusion into the gel and is thus unambiguously a separate step from the initial formation of the
157 yttrium-rich gel phase.

158 To further understand the nature of the gel, we used solid-state nuclear magnetic resonance

159 spectroscopy (SSNMR) to characterize the gel product compared to its eventual fully crystallized
160 α -NaYF product (Figure 4A) as well as orthorhombic YF₃ (Figure 4B). We used orthorhombic YF₃
161 rather than the previously discussed cubic phase because the cubic phase is a metastable product
162 that seems to only form in reactions similar to that reported here, and which literature suggests
163 is nearly impossible to isolate without considerable incorporation of the counteraction from the
164 fluoride precursor.^{35,36} As shown in ¹⁹F spin-echo magic angle spinning (MAS) NMR (Figure 4C)
165 the gel exhibits a broad resonance centered at -61 ppm with a peak width of 30 ppm. As reported
166 by Bessada, et al.,³⁷ the ¹⁹F chemical shift is highly sensitive to its coordination environment in
167 molten fluoride mixtures, displaying a nonlinear and monotonous increase from -225 ppm to -28
168 ppm by increasing the concentration of YF₃ from 0 to 100% in the NaF-YF₃ mixture. Compared
169 to orthorhombic YF₃, which shows a relatively sharper peak at -58 ppm with a width of 12 ppm,
170 and α -NaYF, which has a similarly broad resonance at -77 ppm with a width of 28 ppm, these
171 data are again consistent with a gel that consists of some regions that are more similar to YF₃ and
172 others that are closer to NaYF₄. Because the broadness of the NaYF ¹⁹F spectrum can be attributed
173 to a large distribution of isotropic chemical shifts due to the random arrangement of Na⁺ and Y³⁺
174 around F⁻,^{38,39} we show T₂-filtered ¹⁹F spectra in Figure 4D, which reduce signals from faster-
175 relaxing components and thereby allow for finer resolution of the remaining signal. The respective
176 deconvolution of the resonances reveal that the gel does have some components similar to those in
177 α -NaYF and YF₃ (-81 ppm and -69 ppm, respectively), however the main peaks in the region where
178 we would expect to observe YF₃ are not consistent with the major peak of orthorhombic YF₃ at 58
179 ppm, due to the variation in the coordination geometries of bridging fluoride ions between the cubic
180 and orthorhombic polymorphs of YF₃ as well as amorphous regions. This emphasizes that the YF₃
181 product in the gel is not the orthorhombic phase but rather cubic and amorphous YF₃. Furthermore,
182 Figure 4E shows that the ¹⁹F spin-lattice relaxation time constant T₁ drops significantly from 19
183 s for α -NaYF and 9.2 s for orthorhombic YF₃ to 3.2 s for the gel, which indicates that the major
184 fluoride species are more mobile and less ordered in the gel phase. This is consistent with our

185 observation that there are significant amorphous, poorly crystalline, and disordered regions in the
186 gel and also emphasizes the propensity for this material to undergo solid-state diffusion, as we
187 have observed. Single-pulse ^{23}Na NMR spectra of the gel and the α -NaYF samples, respectively
188 (Figure S6), both contain major resonances centered at -18 ppm and -9.5 ppm, which were assigned
189 respectively to Na^+ sites in the bulk nanoparticles, and to Na^+ sites at the surface or near defects,
190 as originally reported by de Queiroz, et al.³⁹ The fraction of the -9.5 ppm peak changes from 35%
191 in α -NaYF to 75% in the gel sample, suggesting that the gel has over twice as many surface or
192 defective Na^+ sites as compared to the final crystalline product.

193 Thus far, we have shown clear evidence of crystallization following the formation of an
194 amorphous phase as well as of the solid-state diffusion of ions following the initial separation.
195 This is consistent with the many well-characterized two-step crystallization mechanisms in which
196 the initial separation occurs via a DLP, likely formed by SD. To model preliminary ion segrega-
197 tion and computationally predict time-scales affiliated with SD, we modified a previously reported
198 model⁴⁰ that solves the multicomponent Cahn-Morral equation for a simplified version of the NaYF
199 system. The Cahn-Morral equation is a multicomponent analogue to the Cahn-Hilliard equation
200 that describes the dynamics of phase separation and coarsening in a binary mixture.^{13,41} SD phase
201 separation is characterized by clustering of species so that diffusion occurs “up” concentration gra-
202 dients, rendering the classical diffusive transport models ill-posed. Spinodal phase separation is
203 limited by a thermodynamically-modified diffusion process that includes contributions from com-
204 positional gradients in the free energy of the system and, hence, in the chemical potential of each
205 species. Including contributions from compositional gradients in the free energy of the system and
206 in the chemical potential of each species guarantees a well-posed model of diffusion allowing for
207 diffusion up gradients in composition characteristic of SD meanwhile bounding the magnitude of
208 composition buildup. The main parameters that affect the dynamics of the phase separation are the
209 modified chemical potentials of the individual components, including thermodynamic parameters

210 characterizing the homogeneous free energy density and the phenomenological gradient energy
211 coefficients, and the diffusion coefficients of each species in the system. As a first-order approxi-
212 mation, we modeled each individual ion in the reaction $4NaF + YCl_3 \rightarrow NaYF_4 + 3NaCl$ as
213 its own component in the same proportions as in the stoichiometric reaction, all with a diffusion
214 coefficient of $1.4 \times 10^{-5} \text{ cm}^2 \text{ s}^{-1}$, which is an average of the actual aqueous diffusion coefficients of
215 each ion. While this model clearly represents only a first-order approximation of the system, it
216 does allow us to approximate that the system takes about 250 μs to reach a relatively steady state at
217 standard conditions (Figure 5A). Furthermore, by considering the time-resolved model from 0-250
218 μs (Figure 5B), it becomes readily apparent that regions of high or low concentration of various
219 components can form and disappear prior to reaching a steady state, as marked by asterisks in the
220 plots. There are some shortcomings to this modelling approach, the most obvious being that it does
221 not include electrostatic interactions between ions. Furthermore, the separation of the phases from
222 solution cannot be fully separated from simultaneous nucleation and solid-state diffusion phenom-
223 ena. This intricacy illustrates the most intriguing aspect of this ternary NaYF system, namely, that
224 its formation cannot be viewed purely as a two-step nucleation and growth mechanism. Rather, the
225 gradual solid-state diffusion must be thought of as a fundamental part of the overall growth path-
226 way. Future work will combine molecular dynamics simulations with our classical modeling in
227 order to create a more comprehensive model that considers additional electrostatic contributions.

228 This multi-step crystal growth mechanism is not only interesting in its own right, but it also
229 opens the door for further applications of NaYF and similar materials that take advantage of its
230 high surface area. For example, NaYF-gel materials could be useful for future energy storage ap-
231 plications^{30,42} as well as for anti-reflective coatings.⁴³⁻⁴⁵ Anti-reflective coatings are a particularly
232 interesting application because of the possibility employing the optical refrigeration properties of
233 NaYF to actively cool the surface.^{26,46} In preliminary experiments we observe optical refrigeration
234 of the NaYF gel when doped with 10% ytterbium. Our measurements of this gel indicate that it can

235 be laser cooled by approximately 0.55°C and it does not heat under laser irradiation (Figure S7),
236 indicating that it may be a good candidate for actively-cooled anti-reflective coatings, especially
237 due to its lack of organic ligands on the surface, as the effective cooling efficiency of a nanocrystal
238 is reduced by the heating of organic species on the surface^{47,48}.

239 **Conclusions**

240 Crystal nucleation and growth are often described based on the simple addition of monomer units
241 from solution. These depictions of the process typically do not take into account the fact that both
242 the monomer units and the formed solid can and do undergo compositional and structural changes.
243 We have shown that upon the mixture of NaF and YCl₃ in water, a gel separates from solution
244 which then undergoes crystallization, similar to many other two- or three-step crystallization sys-
245 tems. However this system also includes an additional step of solid-state diffusion, where the
246 product initially resembles cubic YF₃ but then undergoes a gradual change of chemical stoichiom-
247 etry to form NaYF over the course of several hours. We anticipate that this multi-step mechanism
248 is not specific to NaYF and more research is needed into other chemical systems where aspects of
249 crystal growth is understood best through more complex nucleation and growth pathways.

250 **Methods**

251 **Synthesis of NaYF gel** The gel is synthesized by mixing a 0.2 M YCl₃ solution with a 0.8 M NaF
252 solution in nanopure water. The mixture is then inverted to fully blend. The gel is then poured into
253 a Büchner funnel with filter paper over vacuum either immediately after mixing or after waiting
254 a specified amount of time (as in the ion replacement experiment), rinsed with water and ethanol,
255 respectively, and allowed to fully dry.

256 **Ion Replacement in Gel** The gel is synthesized as described above and allowed to incubate in its
257 original solution for a period of time, t_{inc} . After t_{inc} has passed, the sample is filtered as described
258 above and rinsed with nanopure water, and the product is resuspended in a solution of 1M KF. This
259 mixture is vortexed until it appears uniform and is allowed to settle overnight. After fully settling,
260 the product is centrifuged and washed with water and ethanol respectively and oven-dried.

261 **Powder X-Ray Diffraction** Powder X-Ray Diffraction (XRD) samples were prepared by drop-
262 casting a concentrated slurry of the sample onto $\langle 100 \rangle$ silicon wafers. XRD spectra were taken on
263 a Bruker D8 Discover Microfocus diffractometer with a Dectris Pilatus3 R 100K-A 2D detector
264 and a Cu $K\alpha$ X-ray source with a 0.5 mm collimator. A Coupled $2\theta/\theta$ scan was performed from
265 16° to 93° with a 5.5° increment to create overlap, with a scan time of 30 seconds per θ . During the
266 scans, the sample was oscillated in the x, y, and ϕ directions to remove the effects of texture and
267 improve statistics. An air scatter screen was used to reduce background. Scans were integrated,
268 indexed, processed, and analyzed using Bruker Diffrac.Eva software.

269 **TEM** TEM images were taken on FEI G² TECNAI F20 S/TEM instruments at 200 kV with ei-
270 ther a Gatan Ultrascan CCD or an FEI Eagle CCD camera. Images were processed using Gatan
271 Digital Micrograph (DM) and Tecnai Imaging and Analysis (TIA) software. STEM Tomographic
272 reconstructions were compiled using FEI Inspect3D software, using a simultaneous iterative re-
273 construction technique (SIRT) with 50 iterations. These reconstructions were then visualized us-
274 ing IMOD.⁴⁹ Scanning transmission electron microscopy (STEM) bright field (BF) imaging and
275 STEM-energy dispersive x-ray spectroscopy (EDS) were performed in a Nion UltraSTEM-X oper-
276 ated at 60 kV. The microscope is equipped with a Bruker XFlash windowless silicon drift detector,
277 and EDS data were analyzed using Bruker Esprit software. The NaYF samples were dispersed in
278 ethanol and dropcast onto Cu TEM grids with lacey carbon films.

279 **Computational methods** The TEM spatial FFT analysis was performed using a homebuilt Python
280 script. To determine the scale, the code optically detected the scale bar printed on the image by
281 the TEM software (Tecnai Imaging and Analysis) and a calibration factor of 22.800 pixels/nm was
282 obtained. Points on the image were manually selected, and a region of 100 px x 100 px centered
283 on that point was isolated. From this point the script was set up to perform automated calculations.
284 2D-FFT was performed for each region, followed by a Gaussian background subtraction to enhance
285 the peaks in the reciprocal space. Several filters and masks were applied on the intensity to obtain
286 the peak locations, which was used to determine d-spacing in the inverse space. All detected peaks
287 were organized into a histogram based on measured d-spacing, and the region corresponding to the
288 111 peak for both α -NaYF and cubic YF₃ was isolated (3.00-3.16 Å), with all other measured peaks
289 discarded. A weighted average was performed on the remaining peaks with their peak intensity
290 as respective weights. This resulted in a single d-spacing value associated with each region. This
291 value was then mapped onto a gradient and displayed as a circle at the center of each region on
292 the TEM image. SD was simulated with a Matlab code modified from the original written by
293 Tavakoli.⁴⁰ All codes are available for public use upon reasonable request.

294 **NMR** ¹⁹F and ²³Na magic angle spinning (MAS) NMR spectra were collected on a Bruker Avance
295 III spectrometer with a field strength of 600 MHz (14.1 T, corresponding to 564.71 MHz for ¹⁹F
296 and 158.75 MHz for ²³Na) using 2.5 mm Bruker rotors at a spinning speed of 32 kHz. The regular
297 90° pulse width was 3.1 μs for ¹⁹F and 2.9 μs for ²³Na. ¹⁹F spin-lattice relaxation times (T₁) were
298 measured using the inversion-recovery method (180° - τ_{delay} - 90°- acquisition), and spin- spin
299 relaxation times (T₂) using the Carr-Purcell-Meiboom-Gill (CPMG) method (90°- τ_{delay} - [180°-
300 τ_{delay}]_n - acquisition) after 2 – 96 π-pulses with an interpulse delay time τ_{delay} = 62.5 μs, which was
301 synchronized to the spinning speed of 32 kHz. The spin-echo ¹⁹F spectra were acquired after two
302 rotor cycles with an interpulse delay of 31.25 μs. Single-pulse ²³Na spectra were acquired with a
303 hard RF pulse with a π/20 flip angle of 0.58 μs, while soft RF pulses (90° pulse width at 15 μs) was

304 used for preferentially exciting central transitions in the inverse- recovery experiments. Relaxation
305 delays of $5 \times T_1$ (60 – 200 s for ^{19}F and 1 – 2 s for ^{23}Na) were used in all experiments to ensure the
306 full relaxation of all samples. The ^{19}F chemical shift references were $\text{CF}_3\text{CH}_2\text{OH}$ at -76.55 ppm
307 and solid NaF at -224 ppm as a second reference. ^{23}Na chemical shifts were referenced to 1 M
308 NaCl aqueous solution at 0 ppm.

309 **Data availability**

310 The data that support the findings of this study are available from the corresponding author on
311 reasonable request.

312 **Code availability**

313 All codes or algorithms used to generate results in this study are available from the corresponding
314 author on reasonable request.

315 **References**

316 **References**

- 317 1. Loh, N. D. *et al.* Multistep nucleation of nanocrystals in aqueous solution. *Nature Chemistry*
318 **9**, 77–82. arXiv: 1605.04632 (2017).
- 319 2. Zou, Z. *et al.* On the Phase Diagram of Calcium Carbonate Solutions. *Advanced Materials*
320 *Interfaces* **4**, 1600076 (2017).
- 321 3. Bøjesen, E. D. & Iversen, B. B. The chemistry of nucleation. *CrystEngComm* **18**, 8332–8353
322 (2016).

- 323 4. Liu, X. *et al.* Three-step nucleation of metal–organic framework nanocrystals. *Proceedings*
324 *of the National Academy of Sciences* **118** (10 2021).
- 325 5. Gibbs, J. W. On the Equilibrium of Heterogeneous Substances. *American Journal of Science*
326 *and Arts* **16**, 441 (1878).
- 327 6. Cölfen, H. & Antonietti, M. *Mesocrystals and Nonclassical Crystallization* 1–276 (John Wi-
328 ley & Sons, Ltd, 2008).
- 329 7. De Yoreo, J. Crystal nucleation: More than one pathway. *Nature Materials* **12**, 284–285
330 (2013).
- 331 8. Smeets, P. J. *et al.* A classical view on nonclassical nucleation. *Proceedings of the National*
332 *Academy of Sciences of the United States of America* **114**, E7882–E7890 (2017).
- 333 9. Ostwald, W. Studien über die Bildung und Umwandlung fester Körper. 1. Abhandlung:
334 Übersättigung und Überkaltung. *Zeitschrift für Physikalische Chemie* **22**, 289–330 (1897).
- 335 10. Karthika, S., Radhakrishnan, T. K. & Kalaichelvi, P. A Review of Classical and Nonclassical
336 Nucleation Theories. *Crystal Growth and Design* **16**, 6663–6681 (2016).
- 337 11. Vekilov, P. G. in *Kinetics and Thermodynamics of Multistep Nucleation and Self-Assembly in*
338 *Nanoscale Materials* 79–110 (John Wiley & Sons, Ltd, Hoboken, NJ, 2012).
- 339 12. Wallace, A. F. *et al.* Microscopic Evidence for Liquid-Liquid Separation in Supersaturated
340 CaCO₃ Solutions. *Science* **341**, 885–889 (2013).
- 341 13. Cahn, J. W. On spinodal decomposition. *Acta Metallurgica* **9**, 795–801 (1961).
- 342 14. Wang, F. *et al.* Tracking lithium transport and electrochemical reactions in nanoparticles.
343 *Nature Communications* **3**, 1201 (2012).
- 344 15. Wang, X., Chou, I.-M., Hu, W. & Burruss, R. C. In situ observations of liquid–liquid phase
345 separation in aqueous MgSO₄ solutions: Geological and geochemical implications. *Geochim-*
346 *ica et Cosmochimica Acta* **103**, 1–10 (2013).

- 347 16. Lee, J., Park, K., Chang, T. & Jung, J. C. Polymer/probe interaction in probe diffusion
348 through a polymer matrix: methyl red diffusion in poly(vinyl acetate)/toluene solutions.
349 *Macromolecules* **25**, 6977–6979 (1992).
- 350 17. Jiang, H., Debenedetti, P. G. & Panagiotopoulos, A. Z. Nucleation in Aqueous NaCl So-
351 lutions Shifts from 1-step to 2-step Mechanism on Crossing the Spinodal. *The Journal of*
352 *Chemical Physics* **150**, 124502. arXiv: 1812.02892 (2019).
- 353 18. Horn, D. & Rieger, J. Organic Nanoparticles in the Aqueous Phase—Theory, Experiment,
354 and Use. *Angewandte Chemie International Edition* **40**, 4330 (2001).
- 355 19. Bohenek, M., Myerson, A. & Sun, W. Thermodynamics, cluster formation and crystal growth
356 in highly supersaturated solutions of KDP, ADP and TGS. *Journal of Crystal Growth* **179**,
357 213–225 (1997).
- 358 20. Habraken, W. J. E. M. *et al.* Ion-association complexes unite classical and non-classical the-
359 ories for the biomimetic nucleation of calcium phosphate. *Nature Communications* **4**, 1507
360 (2013).
- 361 21. Fedorov, P. P. *Systems of Alkali and Rare-Earth Metal Fluorides* tech. rep. 11 (1999), 1792–
362 1818.
- 363 22. Bard, A. B. *et al.* A Mechanistic Understanding of Nonclassical Crystal Growth in Hydrother-
364 mally Synthesized Sodium Yttrium Fluoride Nanowires. *Chemistry of Materials* **32**, 2753–
365 2763 (2020).
- 366 23. Qiu, P. *et al.* Tuning lanthanide ion-doped upconversion nanocrystals with different shapes
367 via a one-pot cationic surfactant-assisted hydrothermal strategy. *CrystEngComm* **16**, 1859
368 (2014).
- 369 24. Matijevic, E. Preparation and properties of uniform size colloids. *Chemistry of Materials* **5**,
370 412–426 (1993).

- 371 25. Guan, M. *et al.* Multifunctional upconversion-nanoparticles-trimethylpyridylporphyrin-fullerene
372 nanocomposite: A near-infrared light-triggered theranostic platform for imaging-guided pho-
373 todynamic therapy. *NPG Asia Materials* **7**, e205–e205 (2015).
- 374 26. Zhou, X., Smith, B. E., Roder, P. B. & Pauzauskie, P. J. Laser Refrigeration of Ytterbium-
375 Doped Sodium-Yttrium-Fluoride Nanowires. *Advanced Materials* **28**, 8658–8662 (2016).
- 376 27. Zhou, J., Del Rosal, B., Jaque, D., Uchiyama, S. & Jin, D. Advances and challenges for
377 fluorescence nanothermometry. *Nature methods* **17**, 967–980 (2020).
- 378 28. Fernandez-Bravo, A. *et al.* Ultralow-threshold, continuous-wave upconverting lasing from
379 subwavelength plasmons. *Nature Materials* **18**, 1172–1176 (2019).
- 380 29. Ma, Y. *et al.* Mammalian Near-Infrared Image Vision through Injectable and Self-Powered
381 Retinal Nanoantennae. *Cell* **177**, 243–255.e15 (2019).
- 382 30. Hua, X. *et al.* Revisiting metal fluorides as lithium-ion battery cathodes. *Nature Materials*
383 (2021).
- 384 31. Zhu, Y. *et al.* A Composite Gel Polymer Electrolyte with High Performance Based on Poly(Vinylidene
385 Fluoride) and Polyborate for Lithium Ion Batteries. *Advanced Energy Materials* **4**, 1300647
386 (2014).
- 387 32. Nuñez, N. O. *et al.* Synthesis of Spherical Down- and Up-Conversion NaYF₄-Based Nanophos-
388 phors with Tunable Size in Ethylene Glycol without Surfactants or Capping Additives. *Euro-
389 pean Journal of Inorganic Chemistry* **2008**, 4517–4524 (2008).
- 390 33. Thoma, R. E., Hebert, G. M., Insley, H. & Weaver, C. F. Equilibria in the System Sodium
391 Fluoride-Yttrium Fluoride. *Inorganic Chemistry* **2**, 1005–1012 (1963).
- 392 34. Xia, X. *et al.* Hydrothermal Synthesis and Solid-State Laser Refrigeration of Ytterbium-
393 Doped Potassium Lutetium Fluoride (KLF) Microcrystals. *ChemRxiv* (2020).

- 394 35. Zalkin, A. & Templeton, D. H. The Crystal Structures of YF_3 and Related Compounds.
395 *Journal of the American Chemical Society* **75**, 2453–2458 (1953).
- 396 36. Zhao, M., Li, L. & Li, G. Advances of solution chemistry in stabilizing different crystal
397 phases of inorganic nano-compounds. *CrystEngComm* **18**, 9209–9222 (2016).
- 398 37. Bessada, C., Rakhmatullin, A., Rollet, A.-L. & Zanghi, D. High temperature NMR approach
399 of mixtures of rare earth and alkali fluorides: An insight into the local structure. *Journal of*
400 *Fluorine Chemistry* **130**, 45–52 (2009).
- 401 38. Arnold, A. A. *et al.* Structure of NaYF_4 Upconverting Nanoparticles: A Multinuclear Solid-
402 State NMR and DFT Computational Study. *The Journal of Physical Chemistry C* **117**, 25733–
403 25741 (2013).
- 404 39. De Queiroz, T. B. *et al.* Probing Surface Effects on $\alpha\text{-NaYF}_4$ Nanoparticles by Nuclear Mag-
405 netic Resonance. *The Journal of Physical Chemistry C* **124**, 9523–9535 (2020).
- 406 40. Tavakoli, R. Unconditionally energy stable time stepping scheme for Cahn-Morral equation:
407 Application to multi-component spinodal decomposition and optimal space tiling. *Journal of*
408 *Computational Physics* **304**, 441–464 (2016).
- 409 41. Morral, J. & Cahn, J. Spinodal decomposition in ternary systems. *Acta Metallurgica* **19**,
410 1037–1045 (1971).
- 411 42. Breuer, S., Lunghammer, S., Kiesl, A. & Wilkening, M. F anion dynamics in cation-mixed
412 nanocrystalline $\text{LaF}_3\text{:SrF}_2$. *Journal of Materials Science* **53**, 13669–13681 (2018).
- 413 43. Chen, D. Anti-reflection (AR) coatings made by sol-gel processes: A review. *Solar Energy*
414 *Materials and Solar Cells* **68**, 313–336 (2001).
- 415 44. Fujihara, S., Tada, M. & Kimura, T. Controlling Factors for the Conversion of Trifluoroac-
416 etate Sols into Thin Metal Fluoride Coatings. *Journal of Sol-Gel Science and Technology* **19**,
417 311–314 (2000).

- 418 45. Chi, F. *et al.* Sol–Gel Preparation of Ultralow Refractive Index Magnesium Fluoride Optical
419 Films for Broadband Antireflective Coatings. *Nanoscience and Nanotechnology Letters* **4**,
420 441–444 (2012).
- 421 46. Kumar, A. & Chowdhury, A. Reassessment of different antireflection coatings for crystalline
422 silicon solar cell in view of their passive radiative cooling properties. *Solar Energy* **183**, 410–
423 418 (2019).
- 424 47. Epstein, R. I. & Sheik-Bahae, M. *Optical Refrigeration: Science and Applicaitons of Laser*
425 *Cooling of Solids* (2009).
- 426 48. Luntz-Martin, D. R., Felsted, R. G., Dadras, S., Pauzauskie, P. J. & Vamivakas, A. N. Laser
427 refrigeration of optically levitated sodium yttrium fluoride nanocrystals. *Optics Letters* **46**,
428 3797 (2021).
- 429 49. Kremer, J. R., Mastronarde, D. N. & McIntosh, J. R. Computer Visualization of Three-
430 Dimensional Image Data using IMOD. *Journal of Structural Biology* **116**, 71–76 (1996).

431 **Acknowledgements**

432 We thank R. Stroud and B. Hudak for their help in coordinating and analyzing TEM measurements
433 and preparing the manuscript, and C. Mundy for helpful discussion regarding nucleation theory.
434 Crystal growth studies based on TEM, XRD, NMR, BET, and subsequent analyses and interpreta-
435 tions were performed with support from the U.S. Department of Energy, Office of Science (DOE),
436 Basic Energy Sciences (BES), Division of Materials Sciences and Engineering at the University
437 of Washington (UW) and the Pacific Northwest National Laboratory (PNNL). NMR experiments
438 were performed using EMSL (grid.436923.9), a DOE Office of Science User Facility sponsored
439 by the Office of Biological and Environmental Research. STEM-EDS measurements were per-
440 formed with support from Naval Research Laboratory 6.1 base program funding. XRD and TEM

441 measurements were conducted at the Molecular Analysis Facility, a National Nanotechnology Co-
442 ordinated Infrastructure site at the University of Washington, which is supported in part by the
443 National Science Foundation (grant ECC-1542101), the University of Washington, and the Insti-
444 tute for Nano-engineered Systems (NanoES). Cryo-TEM measurements in the supplement were
445 conducted on an instrument purchased with support from the National Institutes of Health, award
446 number S10OD032290.

447 **Author contributions**

448 R.G.F., A.B.B., and P.J.P. conceived the idea, designed the experiments, and performed synthesis
449 of the materials. A.B.B. performed TEM imaging and STEM tomography. A.B.B., R.G.F., and
450 A.S.G. performed BET measurements. R.G.F. performed XRD measurements. A.P., C.G., and
451 E.N. wrote and implemented the codes used to analyze TEM FFTs. A.S.G. performed EDS mea-
452 surements. Y.C. performed NMR measurements. L.N.B. modified the Cahn-Morral code. B.J.
453 performed TEM measurements. N.M.W., J.J.D.Y., J.C., and L.N.B. provided useful expertise and
454 data interpretation. A.B.B. drafted the manuscript. P.J.P. supervised the research. All authors
455 provided useful discussion and approved the final manuscript.

456 **Competing Interests** The authors declare that they have no competing interests.

457 **Correspondence** Correspondence and requests for materials should be addressed to Peter J. Pauzauskie.
458 Email: peterpz@uw.edu.

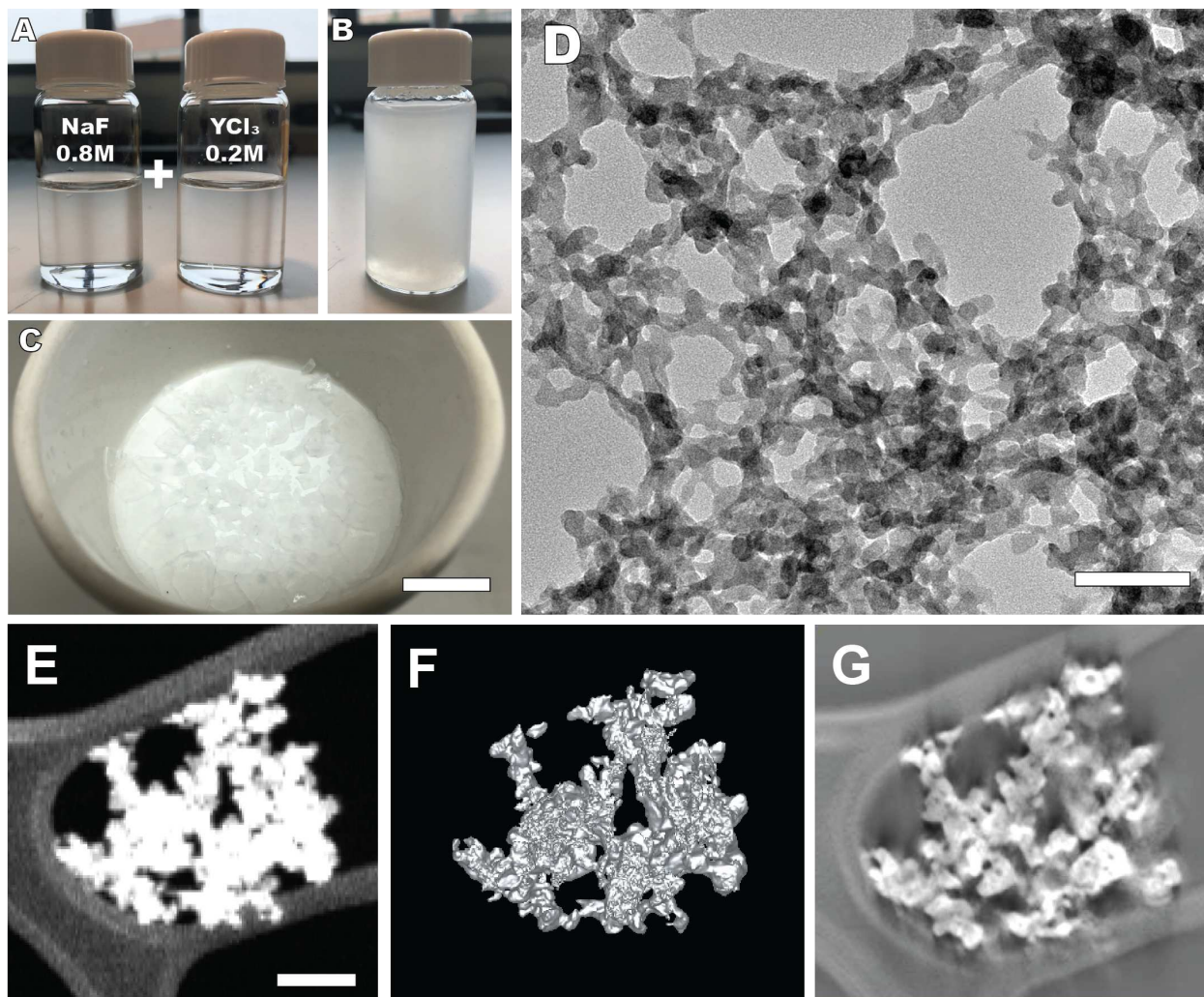


Figure 1: Synthesis of NaYF gel. (A) Starting solutions of 0.8M NaF and 0.2M YCl₃ combine to form (B) a gel, which is (C) filtered to a translucent solid (scale bar = 1 cm), which shows (D) an interconnected structure in bright field TEM. Scale bar = 50 nm (E) STEM HAADF of a small piece of gel. Scale bar = 100 nm (F) Reconstructed tomographic isosurface model of the same particle in E showing three-dimensional physical structure. (G) Reconstructed tomographic slice through roughly the middle of the same particle showing interconnected, porous internal structure

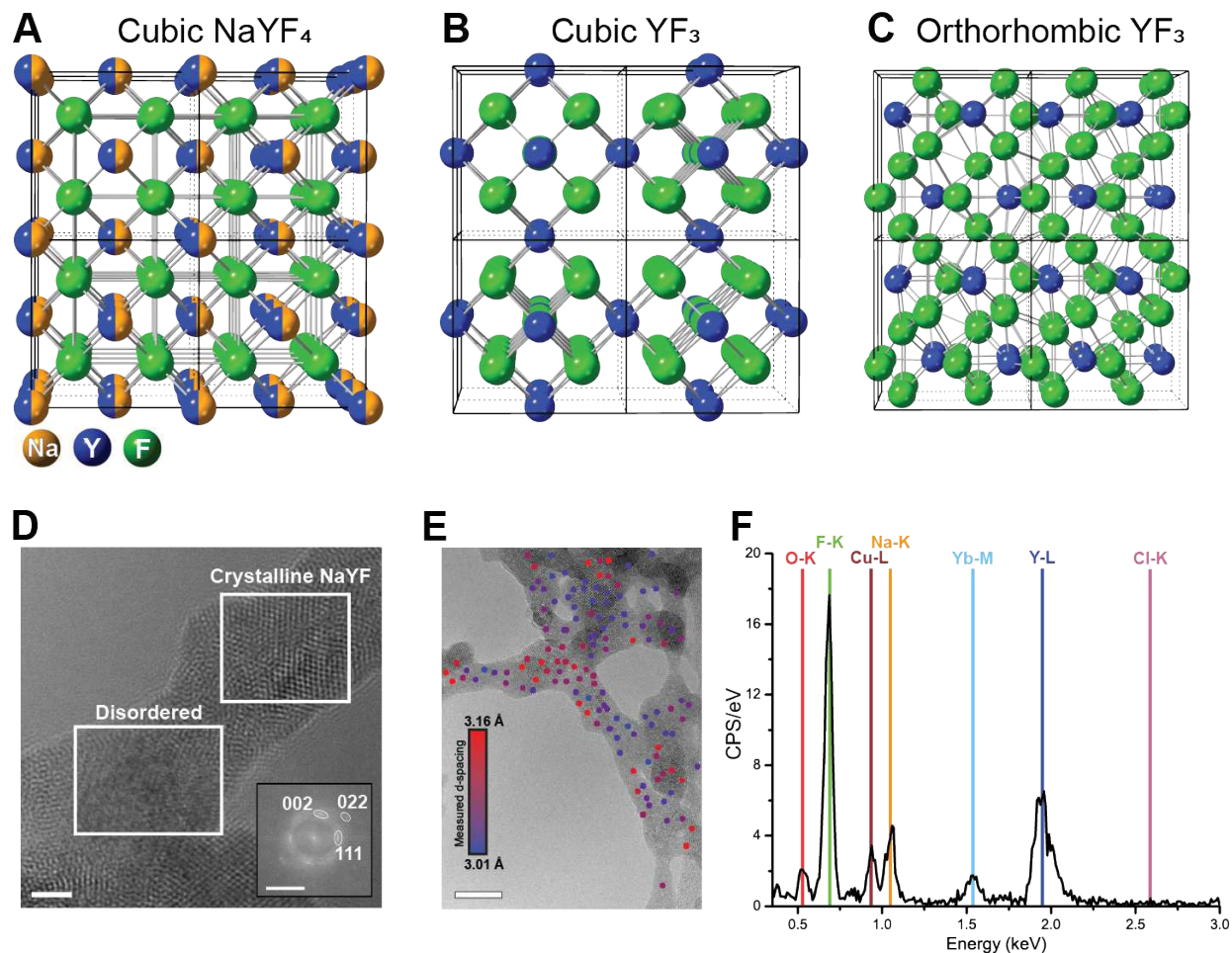


Figure 2: Microstructural characterization of the gel. (A-C) Crystal structures of (A) cubic (α) NaYF₄, (B) cubic YF₃, and (C) orthorhombic YF₃. Yellow = Na, blue = Y, green = F. Each structure shows 2x2 unit cells to emphasize empty space in structure B. (D) Bright field HRTEM of the gel showing both ordered and disordered regions, with an FFT of the labeled ordered region showing it to be cubic NaYF₄ preferentially aligned along the [110] zone axis, with slight misalignment. Scale bar = 5 nm for the TEM and 5 nm⁻¹ for the FFT. (E) Map showing 111 d-spacing measured by FFT, with larger d-spacings shown in red and smaller in blue. Smaller d-spacings correspond to a unit cell closer to NaYF₄ and larger d-spacings correspond to a unit cell closer to YF₃. For more details on the peak assignments, see the supporting information. Scale bar = 10 nm (F) STEM-EDS spectrum showing the elemental analysis. Note the lack of any significant Cl peak. Cu is residual from the TEM grid. STEM-EDS maps are in Figure S5.

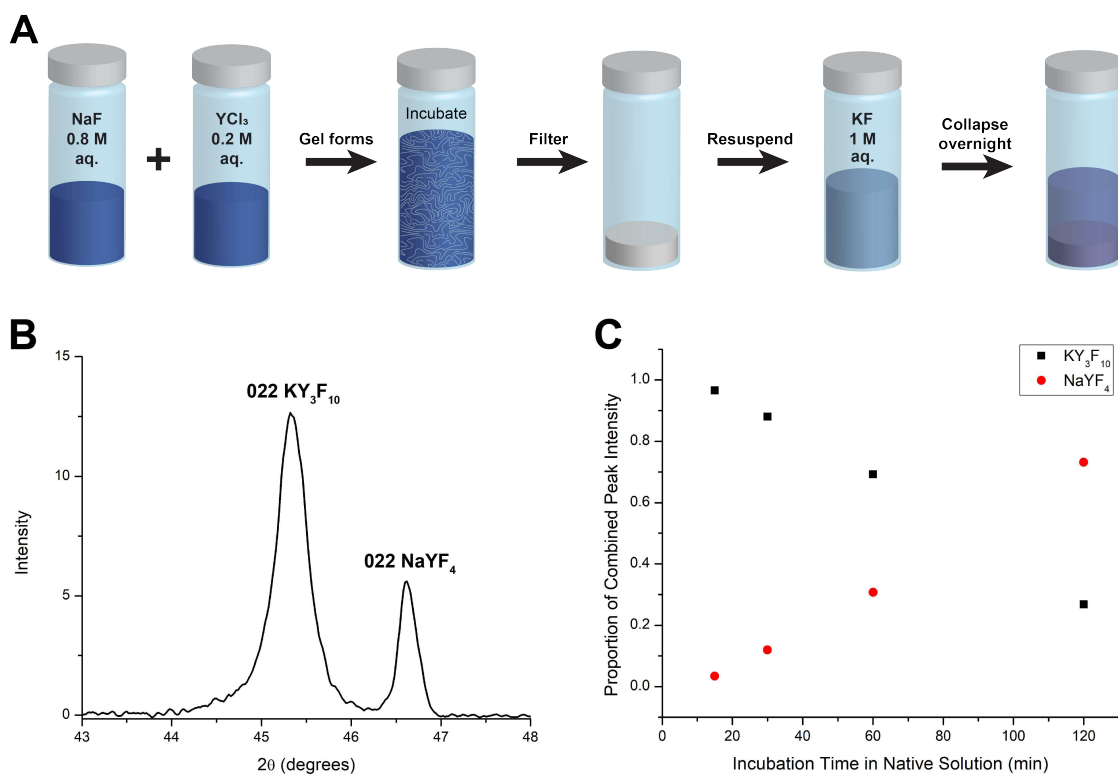


Figure 3: Ion replacement experiment. (A) Schematic for the cation replacement experiment (B) Representative XRD at $t_{\text{inc}} = 60$ minutes zoomed in to show 022 peaks (C) Peak height of the 022 peaks corresponding to either KY_3F_{10} or NaYF_4 normalized to the sum of the 022 peak heights for both phases as a function of t_{inc} . The 022 peak was chosen due to its relatively high intensity as well as the relatively low convolution of the two peaks at that 2θ . This plot shows clearly that the longer the gel is allowed to develop in its native solution prior to filtration, the more sodium is retained by the final product, and the less potassium is incorporated.

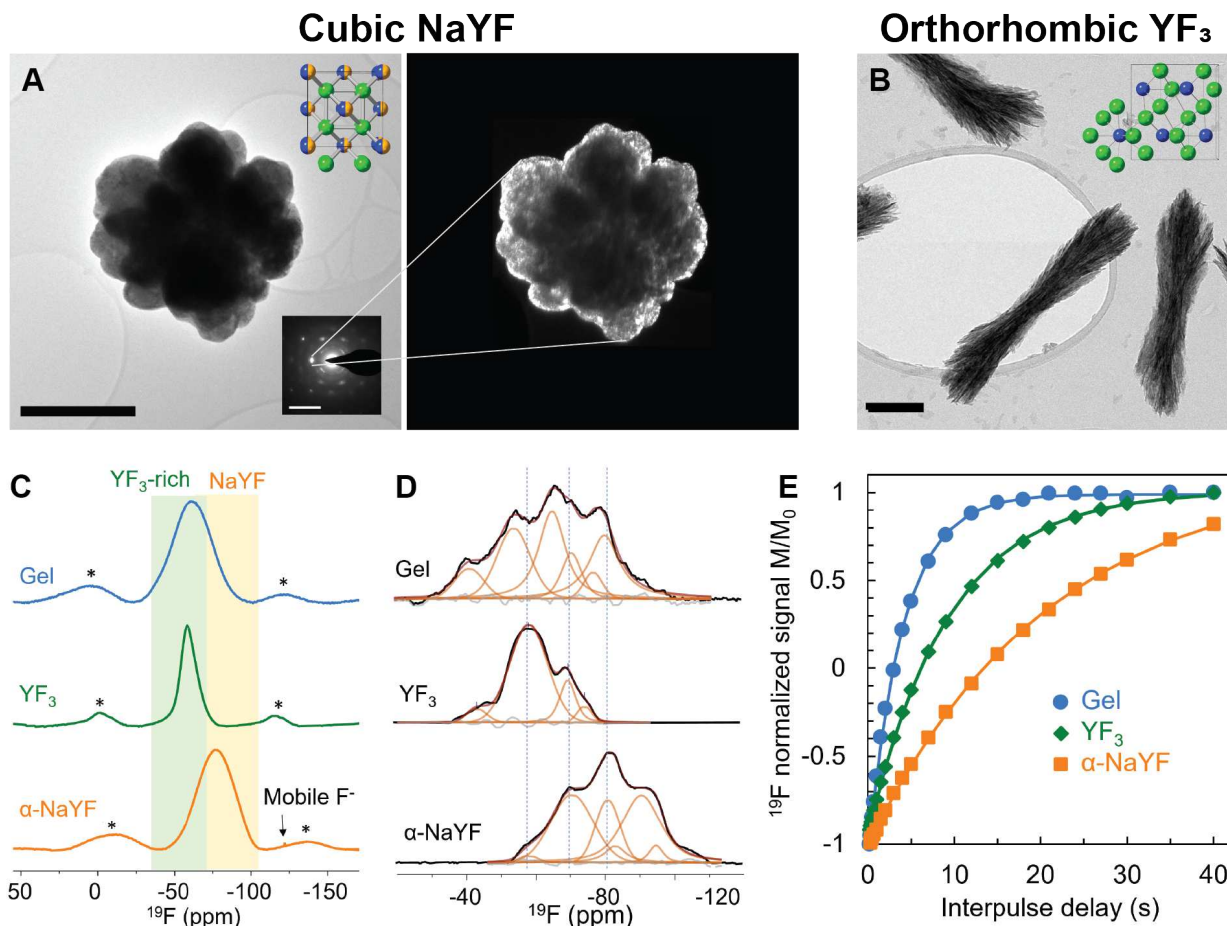


Figure 4: NMR experiments. ¹⁹F solid state NMR comparing the gel with α -NaYF₃ and orthorhombic YF₃ standards at 55C. (A) TEM (left), SAED (bottom inset) and dark field TEM (right) of single-crystalline α -NaYF₃ grown from the gel. The dark field TEM indicates that the whole particle is single crystalline. Top inset shows the α -NaYF₃ crystal structure. Scale bar = 400 nm for the TEM and 5 nm⁻¹ for the SAED. (B) TEM of orthorhombic YF₃ synthesized in a similar, organic-free method. Inset shows orthorhombic YF₃ crystal structure. Scale Bar = 100 nm (C) ¹⁹F spin-echo MAS NMR spectra of the gel, YF₃, and α -NaYF₃ at a spinning speed of 32 kHz and an interpulse delay of 31.25 μ s (one rotor cycle). The asterisks indicate the spinning sidebands. (D) ¹⁹F T₂-filtered NMR spectra of the gel, YF₃, and α -NaYF₃ after eight π -pulses with an interpulse delay of 65.2 μ s (two rotor cycles). (E) ¹⁹F inverse-recovery normalized signal intensity (markers) vs. interpulse delay of gel, YF₃, and α -NaYF₃ as well as the fits (lines) for obtaining the spin-lattice relaxation time constant T₁.

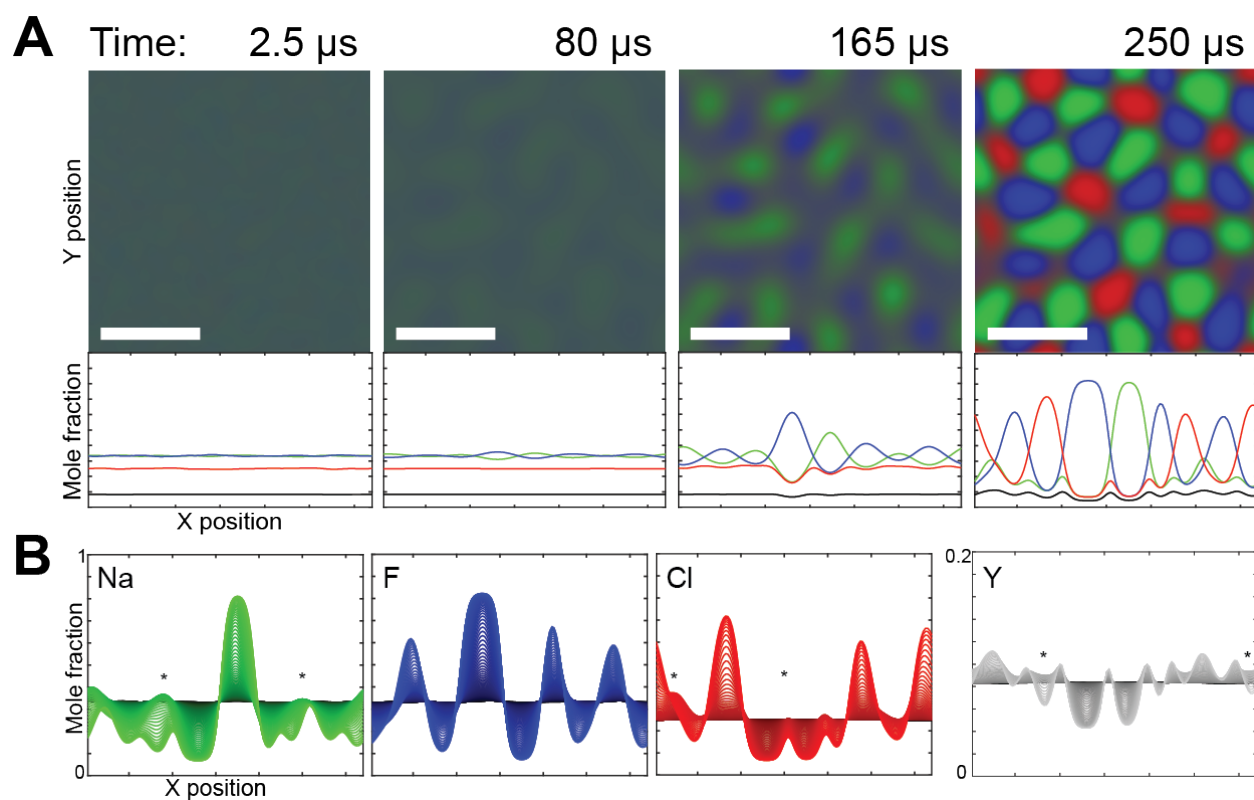


Figure 5: Cahn-Morral modeling. Separation of Na (green), Y (black), F (blue), and Cl (red) ions based on the Cahn-Morral equation and their initial concentrations. (A) Separation of ions at select points over time shown in both two dimensions and one dimension. The one-dimensional plots measure along the horizontal edge of the two-dimensional plots. Time is calculated by measuring an average domain size of 10.708 nm and relating it to a diffusion coefficient of $1.4 \times 10^{-5} \text{ cm}^2 \text{ s}^{-1}$. Scale bar = 10 nm. (B) Evolution of partial composition for each ion, darker colors indicate earlier time points. Note the smaller y axis for the Y plot.

Supplementary Files

This is a list of supplementary files associated with this preprint. Click to download.

- [NYFGSI.pdf](#)